J. Fluid Mech. (1973), *vol.* 60, *part* 1, *pp.* 43–62
Printed in Great Britain

Experiment on convex curvature effects in turbulent boundary layers

By RONALD M. C. SO† AND GEORGE L. MELLOR
Department of Aerospace and Mechanical Sciences, Princeton University,
New Jersey 08540

(Received 26 July 1972 and in revised form 18 January 1973)

Turbulent boundary layers along a convex surface of varying curvature were investigated in a specially designed boundary-layer tunnel. A fairly complete set of turbulence measurements was obtained.

The effect of curvature is striking. For example, along a convex wall the Reynolds stress is decreased near the wall and vanishes about midway between the wall and the edge of a boundary layer where there exists a velocity profile gradient created upstream of the curved wall.

1. Introduction

Reynolds (1884) listed "curvature with the velocity greatest on the outside" as one of four "circumstances conducive to direct or steady motion" but "curvature with the velocity greatest on the inside" as one of four "circumstances conducive to sinuous or unsteady motion". From a description by Prandtl (1929) in an extension of his mixing-length argument one can see heuristically why turbulent flows are sensitive to curvature of the mean flow streamlines. For flows over convex surfaces, the centrifugal 'force' (density × centrifugal acceleration) is largely balanced by a normal pressure gradient. Particles moving outward across mean streamlines into regions of higher mean velocity should on average retain some memory of their previous (lower) mean velocity history; their individual centrifugal forces will be less than the new mean normal pressure gradient, resulting in a net restoring force. Therefore, convex boundary layers should exert a stabilizing influence on turbulent momentum exchange. On concave surfaces, the opposite destabilizing effect should occur. Prandtl also mentioned the apparent analogy between curvature effects and buoyancy effects in a density stratified flow; the latter idea has been developed further by Bradshaw (1969).

Measurements in fully developed curved channels obtained by Wattendorf (1935) and Eskinazi & Yeh (1956) clearly indicated stabilization on the convex side of channels and destabilization on the concave side. Owing to cross-over effects near the channel centre-line, neither effect was clearly isolated, however.

Mean velocity profiles of isolated boundary layers bounded by convex walls

---

† Present address: Geophysical Fluid Dynamics Program, Rutgers University, New Brunswick, New Jersey 08903.

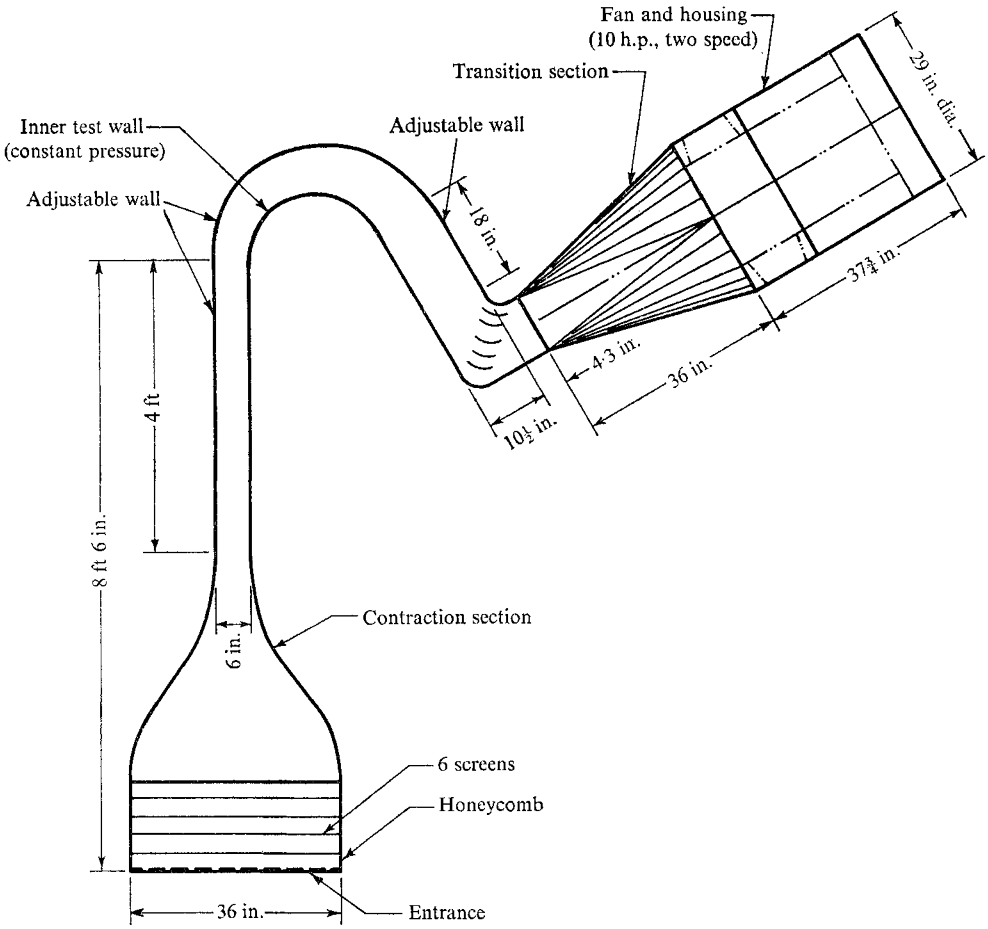

FIGURE 1. A diagrammatic layout of the curved-wall tunnel. The span of the entrance and test section (normal to the page) was 4 ft.

and outer potential flow fields were investigated by Wilcken (1930), Schmidbauer (1936), Schneider & Wade (1967) and Patel (1969*a*). The latter reference also contains an extensive bibliography including curved jet flows.

Generally speaking, both channel flows and boundary-layer flows are obtained in an environment where large-scale secondary flows are present (Patel 1969*b*). The boundary-layer fluid on the end walls of the test channel sweeps from the concave to the convex side resulting in diverging flow on the convex-wall centre-line (see Mellor (1967) for an analytical treatment of this effect). Mainstream pressure gradients can also obscure direct interpretation of curvature effects.

The present experiment was designed to produce isolated boundary-layer flows in an environment where secondary flows have nearly been eliminated and where the mainstream pressure gradient is maintained at a near-zero value. A fairly complete set of turbulence measurements has been obtained so as to provide a relatively direct assessment of the effect of convex curvature on turbulent structure.

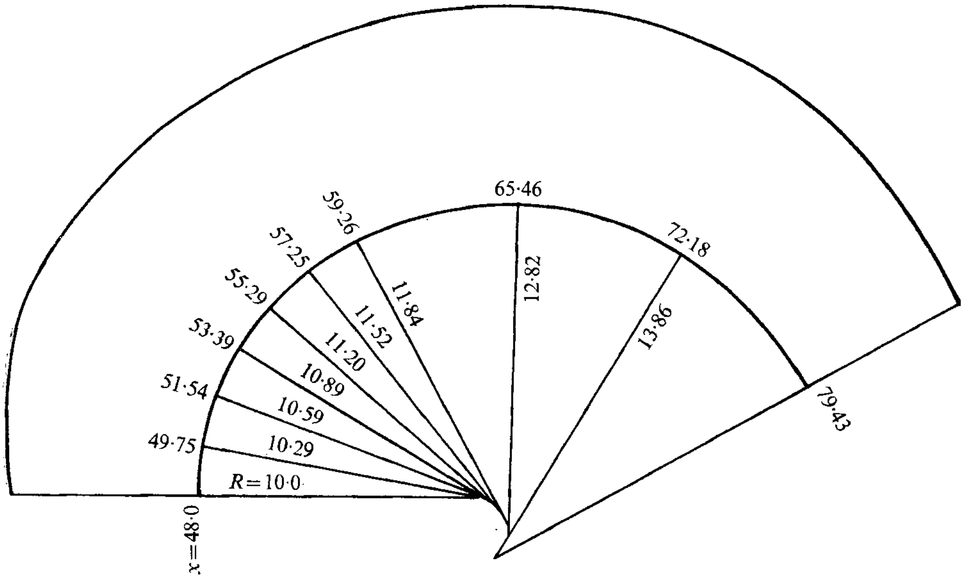

FIGURE 2. Geometry of the curved test section. The convex test wall was made up of sectors of constant radius of curvature. The opposite wall was adjusted to give the nearly constant pressure in the region 50in. $< x <$ 80in. shown in figure 4. All dimensions shown are in inches.

Originally the intention was to obtain a so-called equilibrium boundary layer (Clauser 1954) differing from zero-pressure-gradient data only by virtue of the curvature effect. However, the stabilizing effect of convex curvature itself prevented the attainment of full equilibrium, but as we will see, the turbulence is in a kind of slowly varying equilibrium with the mean velocity profiles and the stabilizing effect of convex curvature on the Reynolds stresses is clearly visible.

2. The experimental apparatus

The curved-wall tunnel used in the present investigation is described in detail by So & Mellor (1972). Briefly, as shown in figures 1 and 2, the wind tunnel is of the open-return suction type and is powered by a two-speed 10h.p. fan. The Reynolds number based on the reference entrance test velocity is $4{\cdot}37 \times 10^5\,\mathrm{ft}^{-1}$. The inlet section of the tunnel consists of several layers of honeycomb flow-straighteners followed by a two-dimensional 6 to 1 contraction chamber. The straight section that follows is 4ft long and has a cross-section 6in. by 48in. The remainder of the tunnel consists of the curved test section, which has a fixed convex test wall of slightly varying curvature and an adjustable opposite wall, followed by the exit diffuser and the fan and motor housing. The adjustable wall permits some control of the pressure distribution on the curved test wall.

In designing the curved wall, an original object was to achieve an equilibrium constant-pressure profile characterized by a curvature parameter Δ/R, where Δ is the defect displacement thickness (defined below in equation (4*b*)) and R is the

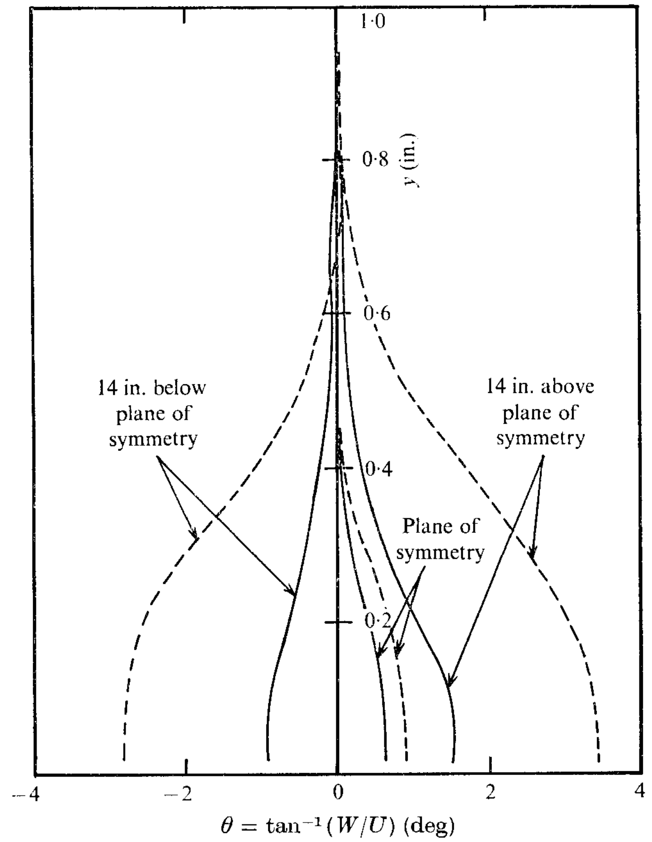

FIGURE 3. Yaw distribution along the convex wall. Measurements were made with a Conrad probe with a diameter of 0·048 in. The solid and broken lines correspond to $x = 54{\cdot}5$ in. and 71 in. respectively.

radius of curvature. To maintain Δ/R constant, $\Delta(x)$ was estimated from flat-plate turbulent formulae and $R(x)$ varied accordingly as detailed in figure 2.

Secondary flows in the curved end-wall regions

In the end-wall regions the centrifugal acceleration of the low velocity boundary-layer flows cannot balance the pressure gradient imposed by the mainstream. The resultant end-wall cross flows or secondary flows create a diverging flow near the tunnel centre-line; the severity of the effect will depend on the aspect ratio. The present tunnel has an aspect ratio of 8 in the straight section and a minimum aspect ratio of 6·2 in the curved test section. To determine the extent of the secondary flow, yaw measurements in the boundary layers were made using a Conrad probe at the tunnel centre-line and at planes 14 in. above and below at $x = 54{\cdot}5$ in. and $x = 71$ in. (For the present study a Cartesian co-ordinate system with x measured along the wall in the flow direction and y normal to the wall was chosen. The origin of x was taken to be at the entrance to the straight section of the tunnel. Therefore, at the entrance to the curved test section, $x = 48$ in.) The probe, which was shaped like a goose-neck, was introduced into the flow through the adjustable wall and its axis was aligned with the radial line at the point of measurement.

Initial measurements revealed that the yaw angles at $x = 54{\cdot}5$ in. were approximately equal and opposite and reached a maximum of $\sim 10^\circ$ at 14 in. on either side of the centre-line while at $x = 71$ in. the maximum was $\sim 20^\circ$. To reduce the secondary flows, eight small end-wall jets were installed on the top and bottom end walls at the entrance to the curved section ($x = 48$ in.). The jets were supplied at a pressure high enough to give critical flow at the jet exits. Thus, the amount of mass flow added to the end-wall boundary layers was quite small, while the amount of momentum added was adjusted to compensate the momentum defect of the end-wall boundary layers and was sufficient to reduce the secondary flow significantly even at $x = 71$ in. With this improvement it can be seen in figure 3 that the flow along the tunnel centre-line was nearly free from the influence of secondary flows.

Further reference to secondary-flow effects are to be found in appendix A.

Pressure distributions on the convex test wall

It was found that the pressure decreased slowly as the flow approached the entrance to the curved section, and then steeply as the flow entered the curved section. The pressure drop amounted to more than 60 % of the reference dynamic head. An effort was made to reduce this pressure drop by increasing the cross-sectional area right at the entrance, but to no avail. Later it was found that the flow was separated on the adjustable wall, right at the entrance to the curved test section. Therefore, increasing the cross-sectional area at this location merely increased the separated region, and the flow on the test wall was undisturbed. To correct this, a 4 ft side-wall jet was installed on the adjustable wall at the entrance to the curved section. The opening of the jet was controlled by a flexible flap attached to the straight wall. The flap extended 8 in. into the straight section, thus providing a certain amount of control on the flow approaching the curved section. Sufficient momentum was supplied to the jet owing to the pressure difference between the outside and inside of the channel. With this arrangement, it was found possible to reduce the pressure drop to 23 % of the reference dynamic head preceded by a small overshoot. After $x \simeq 50$ in. the wall was adjusted to give the nearly constant wall static pressure distribution measured at the tunnel centre-line shown in figure 4. The pressure was measured with reference to the total pressure in the potential core. Wall static pressure at planes 14 in. above and below the tunnel centre-line was also measured. The variations between these measurements and the centre-line measurements were less than 1 % of mainstream dynamic pressure.

It should be noted that the reasonably moderate mainstream acceleration in the region 43 in. $< x <$ 50 in. should not greatly affect the flow when $x > 60$ in. (60 in. – 50 in. $\simeq 80\delta^*$) and should affect it hardly at all when $x > 70$ in.

$$(70\,\text{in.} - 50\,\text{in.} \simeq 150\,\delta^*).$$

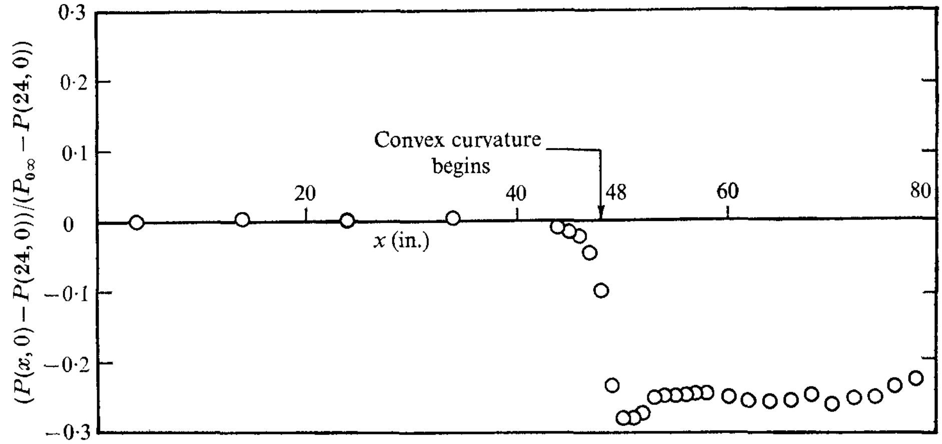

FIGURE 4. Wall static pressure distribution along convex wall. $P_{0\infty}$ is the free-stream stagnation pressure, $P(24,0)$ is the wall static pressure at $x = 24$ in. and $P(x,0)$ is the wall static pressure.

x (in.)	R (in.)	U_{pw} (ft/s)	δ (in.)	δ^* (in.)	θ (in.)	C_f	$q(x)$ (in.^{2})	Δ/R
24·0	∞	70·27	0·55	0·083	0·059	0·00352	0	0
52·5	10·59	78·74	0·95	0·112	0·085	0·00336	0·075	0·258
54·5	10·89	78·87	0·95	0·118	0·087	0·00310	0·072	0·275
56·5	11·20	78·79	0·95	0·125	0·091	0·00290	0·076	0·293
59·0	11·52	78·34	0·95	0·130	0·093	0·00275	0·079	0·304
63·0	11·84	78·66	0·95	0·133	0·094	0·00248	0·077	0·312
67·0	12·82	78·79	0·95	0·146	0·100	0·00243	0·089	0·327
71·0	12·82	78·98	0·95	0·155	0·105	0·00233	0·094	0·353

TABLE 1. Boundary-layer parameters

This assertion can be checked by direct appeal to similar data compiled for the Stanford Computation Conference (Coles & Hirst 1968). We have also checked this point using the computer program of Mellor & Herring (1968), which predicted the Stanford data quite well. For the present initial conditions at $x = 24$ in. and the mainstream velocity distribution of figure 4, but for zero curvature, the computed profiles indicated the re-establishment of zero-pressure-gradient equilibrium at $x = 60$ in.

3. Measurement techniques

A total head probe which was introduced into the flow through the adjustable wall with its axis aligned with the radial line at the point of measurement was used to measure the local stagnation pressure. The accuracy of the total head probe was checked against a standard Pitot-static probe in a fully developed turbulent pipe flow and no discrepancy was found between the two measured velocity profiles. Altogether twelve stagnation pressure profiles were measured, eight along the tunnel centre-line and four on planes 14 in. above and below. The velocity profiles were calculated from the measured stagnation pressure profiles according to the method described in appendix A.

Mean velocity profiles were also obtained in the course of the turbulence measurements. These hot-wire profiles and the Pitot-tube profiles agreed to within 1–2 %.

The principal parameters are presented in table 1. If $U(x,y)$ is the local mean velocity, then from the condition of irrotationality

$$U_p \equiv U_{pw}(x)\,e^{-k(x)y} = U_{pw}[(1-ky)+O(yk)^2] \tag{1}$$

is the potential-flow velocity field and U_{pw} is its value at the wall. (We assume that the normal variation of curvature k is negligible.) The displacement and momentum thicknesses are

$$\delta^* \equiv \int_0^\infty \left(1-\frac{U}{U_p}\right)dy, \quad \theta \equiv \int_0^\infty \frac{U}{U_p}\left(1-\frac{U}{U_p}\right)dy \tag{2a,b}$$

and the skin-friction coefficient is

$$C_f \equiv \tau_w/\tfrac{1}{2}\rho U_{pw}^2. \tag{2c}$$

$q(x)$ is an additional parameter involved in the integral balance as described in appendix A. Δ/R is also listed and is nearly constant in the test region.

The skin friction at the wall was not measured, but was obtained from a Clauser (1956) plot whereby graphs of U/U_{pw} *vs.* $\log(yU_{pw}/\nu)$ are determined from the law of the wall and are parametric in C_f. The line that best fits the experimental points near the wall is taken to give the correct C_f for the measured profile. These values are compatible with a momentum balance discussed in appendix A and with the turbulence measurements shown in figure 13 (*b*).

Turbulence measurements

Generally, measurements of turbulent stresses are made with an x probe or a v probe. However, this method requires accurate alignment of the probe, and this posed serious problems in the present investigation. For this reason a rotating-wire technique proposed by Fujita & Kovasznay (1968) was developed. The method, used also by Bissonnette & Mellor (1971), involves the rotation of the probe stem about its own axis while the centre of the wire is held as a fixed point in the flow. The mean signal is then used to obtain calibrating constants for the turbulent fluctuating signal and in this sense is continuously self-calibrating.

Again, the hot-wire probe was introduced into the flow through the adjustable wall such that the axis of the probe stem was aligned with the radial line at the point of measurement. In order to measure both the turbulence intensities ($\overline{u^2}$, $\overline{v^2}$ and $\overline{w^2}$, where u, v and w are the fluctuating velocity components along the Ox, Oy and Oz axis) and the shear stress ($-\overline{uv}$), two different probe configurations, hereafter called probe A and probe B, were used. With probe A, the sensor rotated in a plane parallel to the tunnel wall (the x, z plane), while with probe B, the sensor rotated in a plane inclined at the complement of the angle the axis of

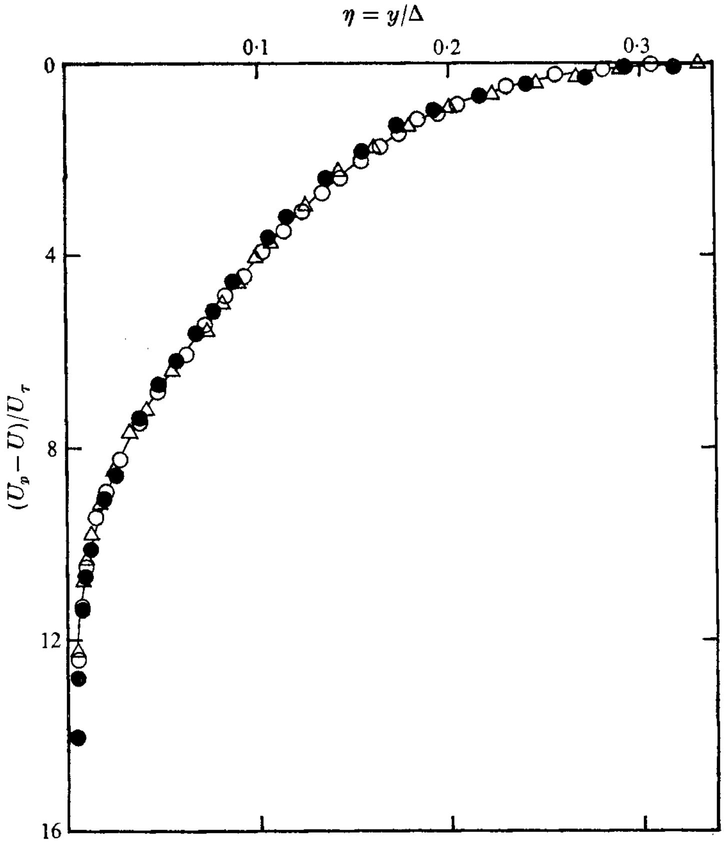

FIGURE 5. Defect plot of flat-plate velocity profiles at $x = 24$ in. Theory: ——, $\beta = 0$, Mellor & Gibson (1966). Measurements: ○, zero-pressure-gradient flow along convex wall; △, adverse-pressure-gradient flow along convex wall; ●, zero-pressure-gradient flow along concave wall.

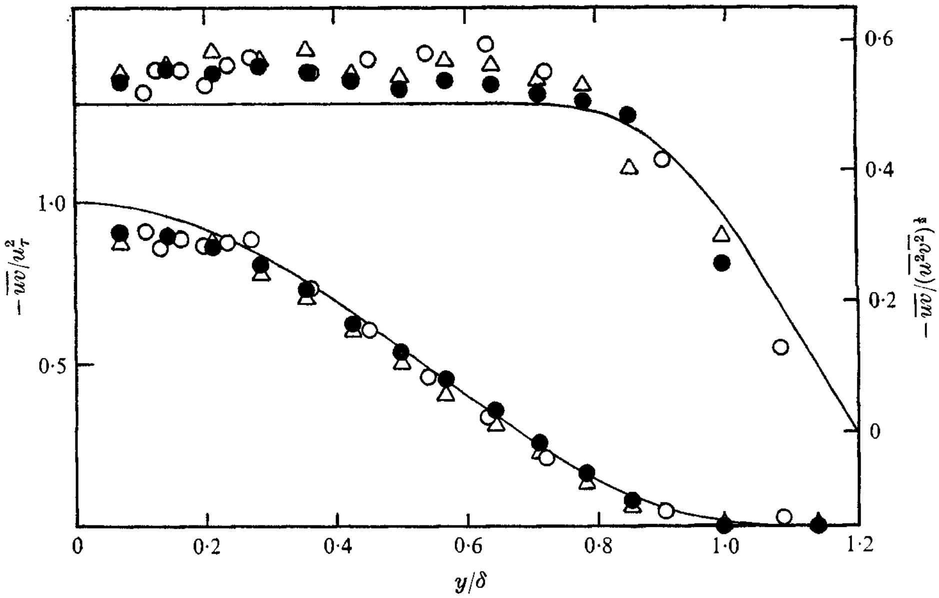

FIGURE 6. Shear stress and correlation distribution of flat-plate boundary layer at $x = 24$ in. ——, Klebanoff (1955); ○, zero-pressure-gradient flow along convex wall; △, adverse-pressure-gradient flow along convex wall; ●, zero-pressure-gradient flow along concave wall.

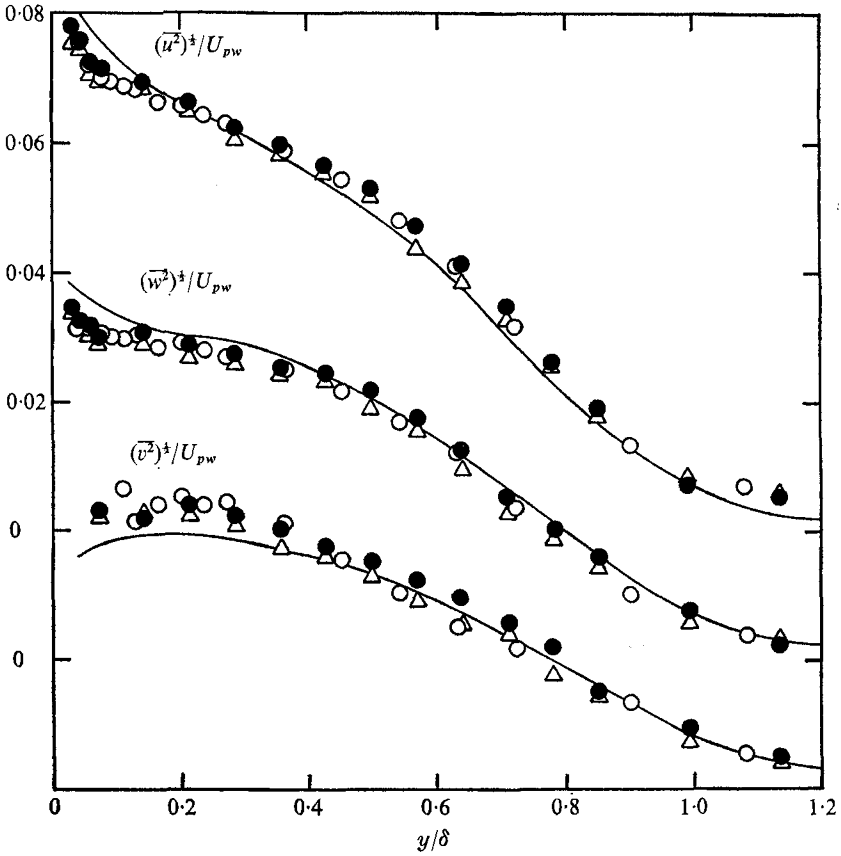

FIGURE 7. Distribution of $(\overline{u^2})^{\frac{1}{2}}/U_{pw}$, $(\overline{w^2})^{\frac{1}{2}}/U_{pw}$ and $(\overline{v^2})^{\frac{1}{2}}/U_{pw}$ for flat-plate boundary layer at $x = 24$ in. ——, Klebanoff (1955); ○, zero-pressure-gradient flow along convex wall; △, adverse-pressure-gradient flow along convex wall; ●, zero-pressure-gradient flow along concave wall.

the probe stem made with the tunnel wall (see figure 17). The hot-wire signals were plotted on X–Y plotters and then digitized for analysis using the data reduction program of Bissonnette & Mellor (1971). Further details of the hot-wire technique are provided in appendix B.

4. The experimental data

Uniformity and steadiness of the flow in the upstream straight section of the tunnel were checked by observing tufts attached to the walls of the tunnel. To establish confidence in the measurement technique the upstream constant-pressure region at $x = 24$ in. was measured and compared with previous data. First, the velocity profile obtained with the flattened total head probe was plotted in figure 5 along with the zero-pressure-gradient profile of Mellor & Gibson (1966), which agreed with a great deal of previous data. This indicates that an equilibrium turbulent flow exists at $x = 24$ in. In figures 6 and 7 the measured $-\overline{uv}/u_\tau^2$,

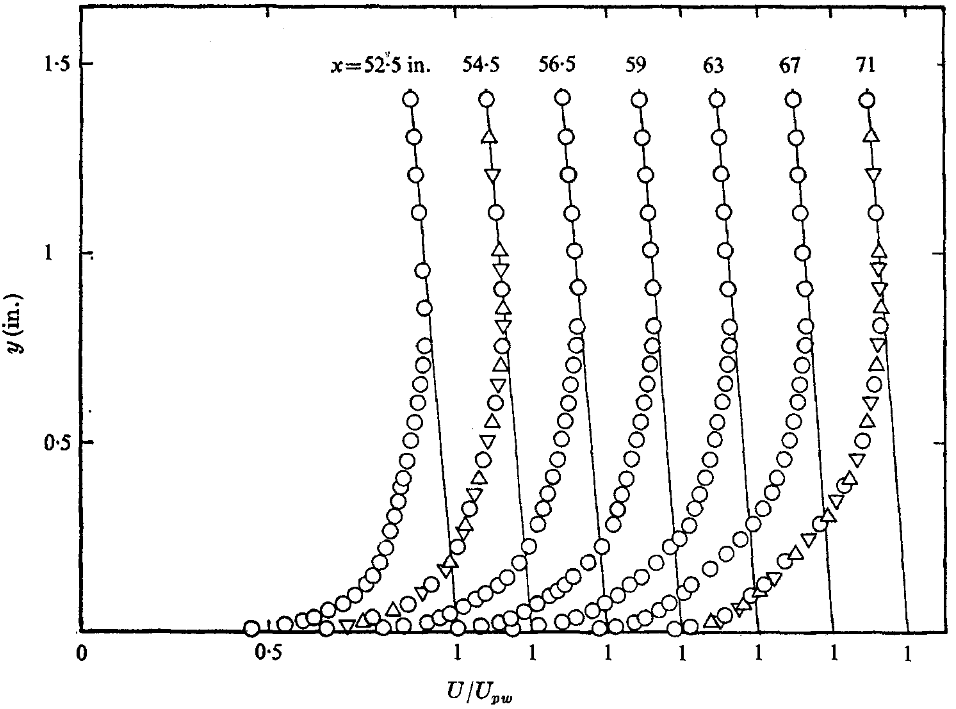

FIGURE 8. Velocity profiles. ○, plane of symmetry; △, 14 in. above plane of symmetry; ▽, 14 in. below plane of symmetry. Potential velocity: ——, calculated from $U_p/U_{pw} = 1-ky$.

$-\overline{uv}/(\overline{u^2}\,\overline{v^2})^{\frac{1}{2}}$, $(\overline{u^2})^{\frac{1}{2}}/U_{pw}$, $(\overline{w^2})^{\frac{1}{2}}/U_{pw}$ and $(\overline{v^2})^{\frac{1}{2}}/U_{pw}$ were plotted against y/δ and compared with the flat-plate data of Klebanoff (1955).

Also shown are data obtained when the tunnel was set up for an adverse pressure gradient together with data obtained when the tunnel was rigged for experiments on the opposite concave wall.†

The flow along a convex wall

The mean profiles were first plotted in linear form in figure 8, which also shows their asymptotic behaviour as $y \to \infty$. In figure 9 the measured velocity profiles were plotted to show the law of the wall region using the u_τ determined from Clauser plots. The profiles deviate from the logarithmic portion of the law of the wall given by

$$U/u_\tau = 5{\cdot}6\log(yu_\tau/\nu)+4{\cdot}9 \tag{3}$$

at about the same point as for the flat-plate profile ($x = 24$ in.).

Generalized for curved flow the defect law can be written as

$$(U_p-U)/u_\tau \equiv F(y/\Delta, x), \tag{4a}$$

---

† The adverse pressure gradient data is available in the original report (So & Mellor 1972) and will not be published elsewhere. The concave data, requiring a considerably different experimental approach, has been prepared for separate publication.

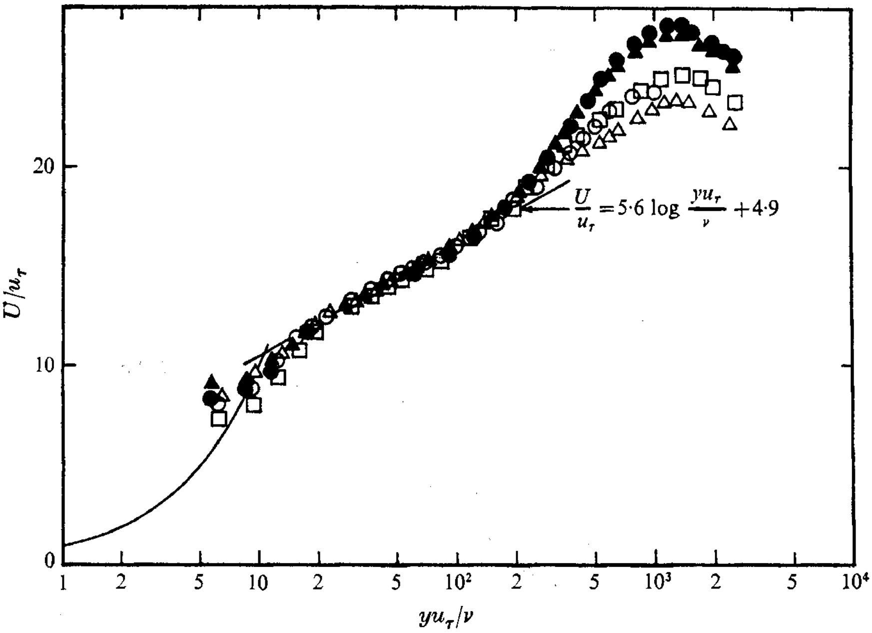

FIGURE 9. Semi-log plot of the velocity profiles to show the law of the wall region. ○, $x = 24$ in.; △, $x = 54{\cdot}5$ in.; □, $x = 59$ in.; ▲, $x = 67$ in.; ●, $x = 71$ in.

where
$$U_p \simeq U_{pw}(1 - y/R),$$

$$\Delta \equiv \int_0^\infty \frac{U_p - U}{u_\tau}\, dy \tag{4b}$$

and
$$F \sim -5{\cdot}6 \log (y/\Delta) + A \quad \text{as} \quad y \to 0. \tag{4c}$$

The velocity profiles are plotted in defect form in figure 10. With the assumption that U can be described equally by (3) or ($4a, b, c$), very near the wall (where $U_p \simeq U_{pw}$), the combination of these two equations yields the skin-friction equation

$$\left(\frac{2}{C_f}\right)^{\frac{1}{2}} \equiv \frac{U_{pw}}{u_\tau} = 5{\cdot}6 \log \frac{U_{pw}\delta^*}{\nu} + 4{\cdot}9 + A, \tag{5}$$

where
$$\Delta u_\tau = U_{pw}\delta^* \equiv U_{pw} \int_0^\infty \left(1 - \frac{U}{U_p}\right) dy.$$

Clauser (1956) pointed out that, for equilibrium flow where

$$\beta = (\delta/\tau_w)\, dp/dx = \text{constant},$$

F and A are independent of x but parametric in β; the function was later calculated by Mellor & Gibson (1966). For curved equilibrium flow one would presume that F and A would be parametric in β and Δ/R.

The turbulence data are presented in figures 11–14. The normalized energy production $-\overline{uv}/u_\tau^3\,(\partial U/\partial y - kU)$ is shown in figure 15. Advection of turbulent energy was not significant; diffusion and dissipation were not measured.

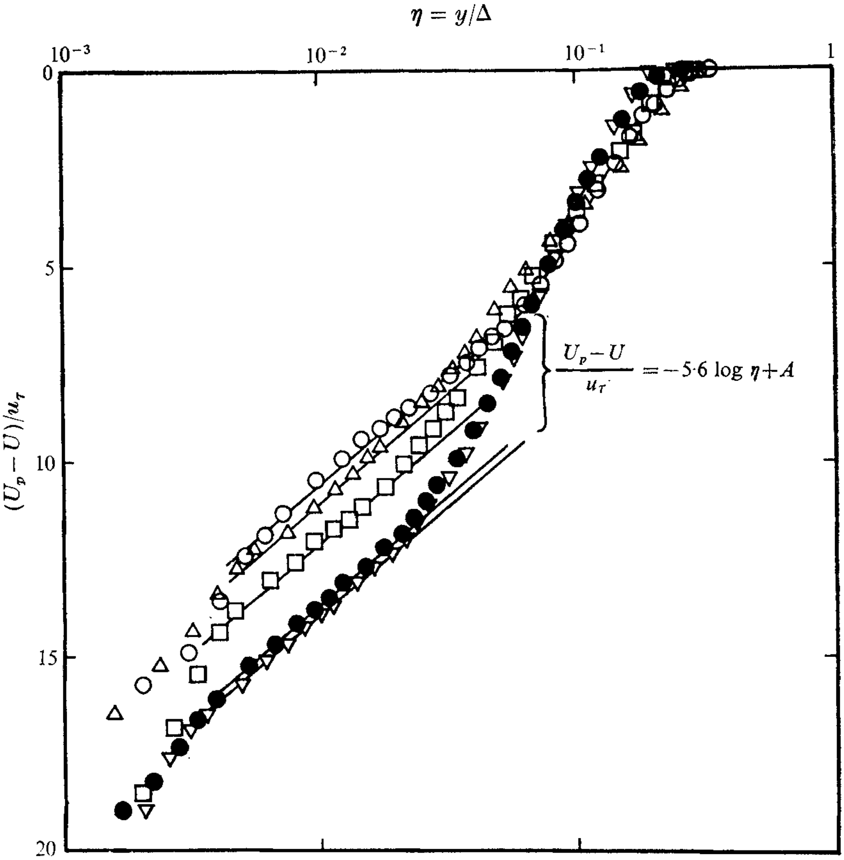

FIGURE 10. Semi-log plot of velocity defects to show dependence of A on curvature. ○, $x = 24$ in., $A = -0{\cdot}59$; △, $x = 54{\cdot}5$ in., $A = -0{\cdot}1$; □, $x = 59$ in., $A = 0{\cdot}9$; ●, $x = 67$ in., $A = 2{\cdot}5$; ▽, $x = 71$ in., $A = 2{\cdot}7$.

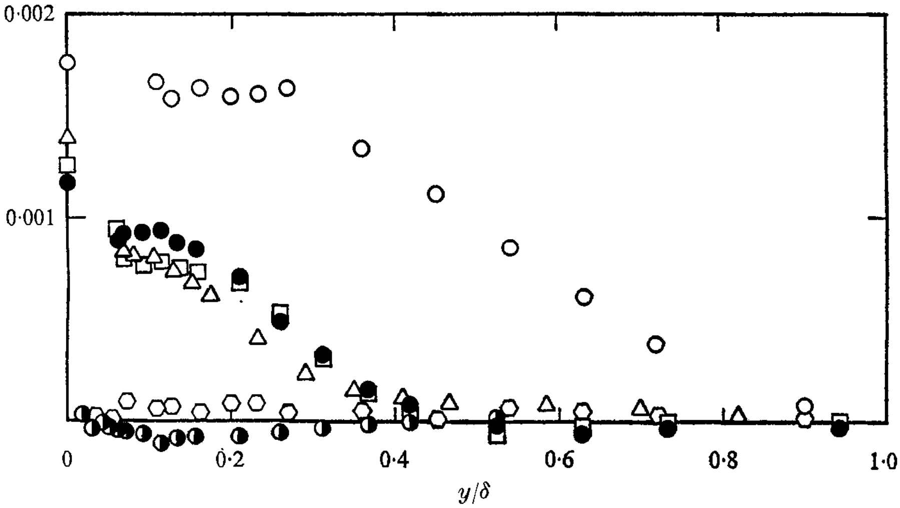

FIGURE 11. Shear stress distribution across the boundary layer. $-\overline{uv}/U_{pw}^2$: ○, $x = 24$ in.; △, $x = 59$ in.; □, $x = 67$ in.; ●, $x = 71$ in. $\overline{uw}/U_{pw}^2$: ○, $x = 24$ in.; ◑, $x = 71$ in. The data points at $y/\delta = 0$ are obtained from the Clauser plots.

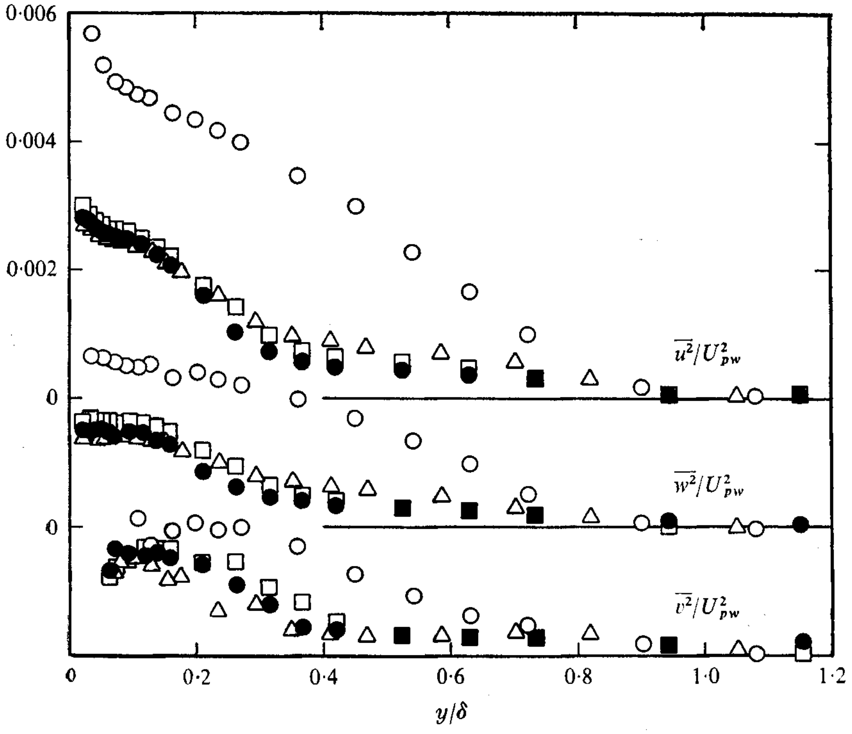

FIGURE 12. Distribution of $\overline{u^2}/U^2_{pw}$, $\overline{v^2}/U^2_{pw}$ and $\overline{w^2}/U^2_{pw}$ across the boundary layer. ○, $x = 24$ in.; △, $x = 59$ in.; □, $x = 67$ in.; ●, $x = 71$ in.

5. Discussion

The wall friction data obtained by the Clauser plots are in agreement with an overall momentum balance described in appendix A, but appear a bit large relative to a wall extrapolation of the hot-wire data in figure 11. However, Bissonnette & Mellor (1971) had previously determined that $-\overline{uv}$ (but not the energy component) data are measured low by the present system roughly when $y/l \lesssim 2$, where l is the wire length. This corresponds to $y/\delta \lesssim 0{\cdot}13$ in figure 11.

Further evidence that curvature does not affect the flow near the wall is contained in figures 13 (*b*) and 15, where the turbulent energy and production normalized by u_τ are similar to the flat-plate data in the wall region

$$(y < 0{\cdot}16\delta \simeq 200\nu/u_\tau).$$

The data at $x = 59$ in. (figure 13*b*) are influenced by the favourable pressure gradient at the entrance to the curved section; however, this influence disappears by the time the flow reaches $x = 67$ in.

Equilibrium was not achieved. This is due primarily to the curvature itself, which has literally 'turned off' the shear stress at $y \simeq 0{\cdot}4\delta \simeq 0{\cdot}4$ in., where the velocity gradient is substantial. The ratio Δ/R increases a bit but this is probably a minor influence. (Note that in figure 12 the scattered deviation of $\overline{uv}$ about zero when $y > 0{\cdot}4\delta$ is about the same as the deviation of $\overline{uw}$ everywhere. This can be taken as the measurement error for the system although agreement of

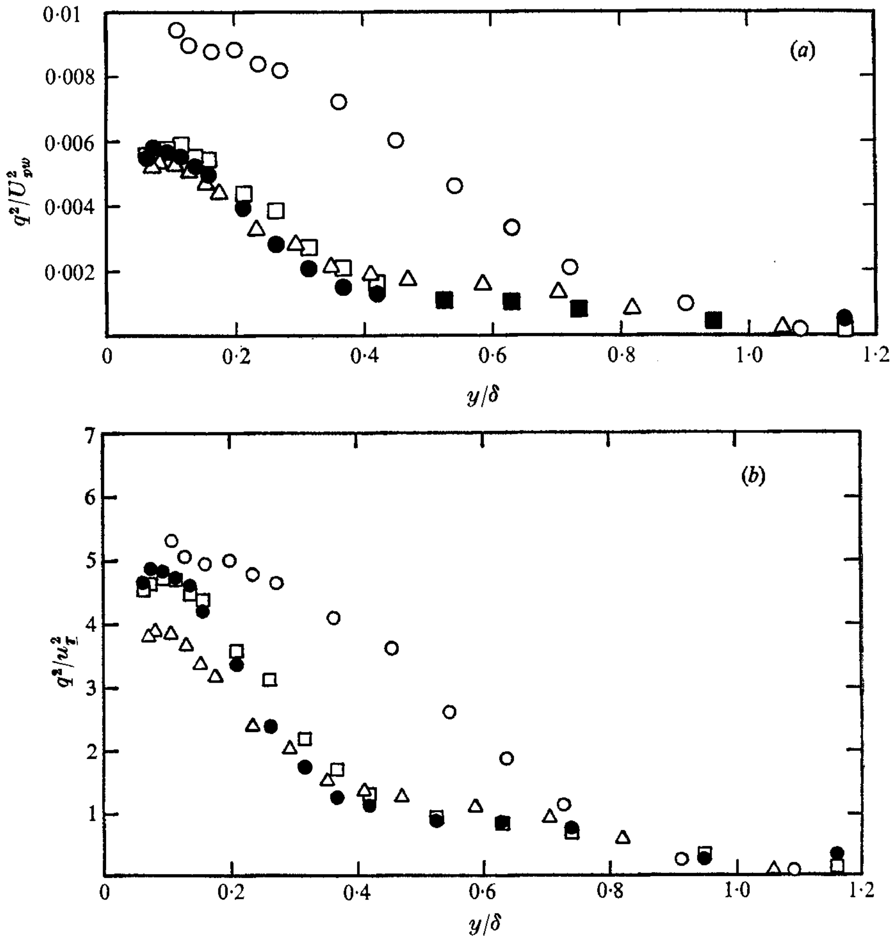

Figure 13. Distribution of turbulence energy across the boundary layer. ○, $x = 24$ in.; △, $x = 59$ in.; □, $x = 67$ in.; ●, $x = 71$ in. (a) q^2/U_{pw}^2. (b) q^2/u_τ^2.

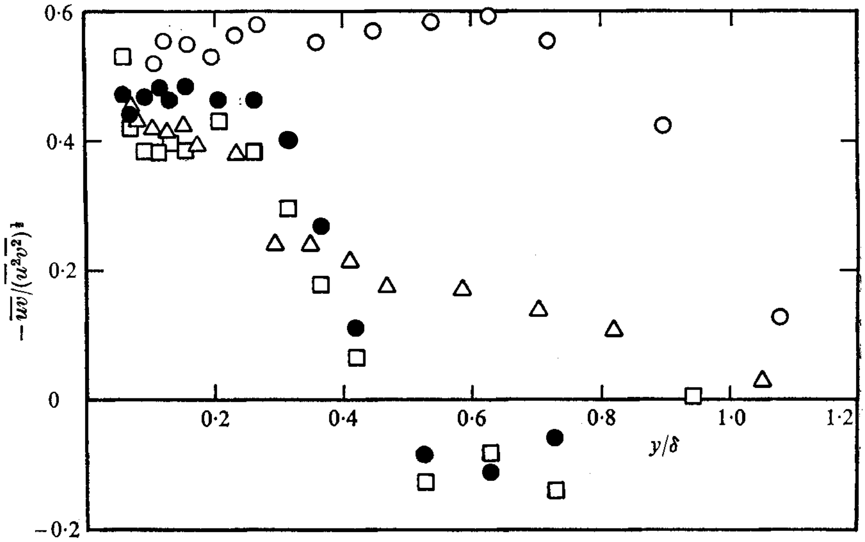

Figure 14. Distribution of shear correlation coefficient across the boundary layer. ○, $x = 24$ in.; △, $x = 59$ in.; □, $x = 67$ in.; ●, $x = 71$ in.

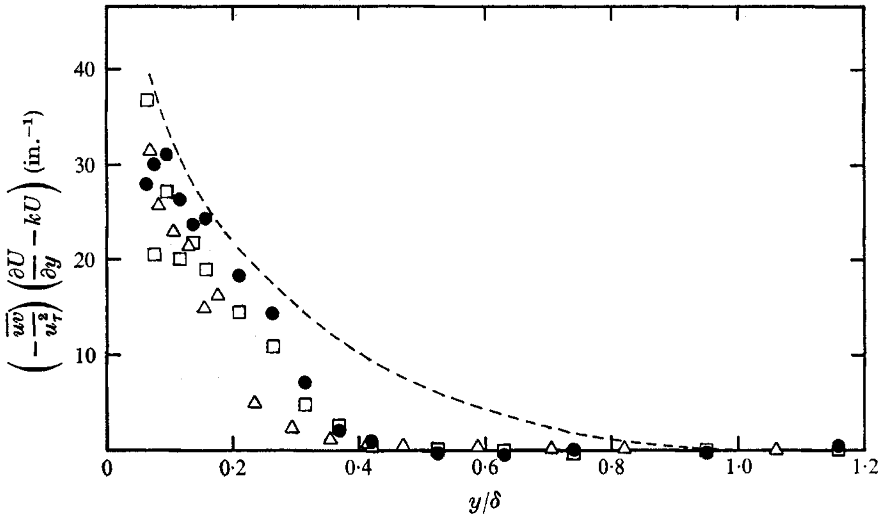

FIGURE 15. Distribution of energy production across the boundary layer. ---, $x = 24$ in.; △, $x = 59$ in.; □, $x = 67$ in.; ●, $x = 71$ in.

the flat-plate $\overline{uv}$ data with Klebanoff's data was somewhat better.) Presumably, if the experiment could have been continued, the edge of the 'Reynolds shear stress layer' would have grown until it coincided with the edge of the 'velocity layer', at which point a true equilibrium boundary layer would have been established.

If one examines the equations for the Reynolds stress tensor (single-point double-velocity correlation equations) one can readily see that the non-dimensional quantity

$$R_i' \cong 2\frac{U/R}{\partial U/\partial y} \tag{6}$$

should describe the relative importance of the curvature effect. Equation (6) was previously suggested by Bradshaw (1969), who heuristically pointed out an analogy between curvature stabilization and buoyancy stabilization in a density stratified boundary layer described by the Richardson number

$$R_i \equiv -\frac{g(\partial\rho/\partial y)}{\rho(\partial U/\partial y)^2}. \tag{7}$$

While we do not believe that the analogy is quite as close as might be construed from Bradshaw's discussion, we nevertheless obtain a value of $R_i' \cong 0{\cdot}30$ at $y/\delta = 0{\cdot}4$ and $x = 71$ in. which can be compared to the value $R_i \cong 0{\cdot}20$ determined by Businger *et al.* (1971) and others as the critical Richardson number beyond which turbulence cannot exist. One might go further and speculate that the low level q^2 signal for $y/\delta > 0{\cdot}4$ (see figures 12 and 13) represents linear 'internal waves' with zero $\overline{uv}$ correlation (figure 14).

In the law of the wall region, say $yu_\tau/\nu = 100$, $R_i' \cong 0{\cdot}035$ and becomes smaller upon further approach to the wall. The data and correlations of Businger *et al.*

would indicate negligible stabilization at equivalent values of R_i in accordance with the present results.

This work was supported by NASA Grant NGR 31-001-74 monitored by S. Lieblein.

Appendix A. Pitot flow field measurements and the integral momentum balance

To be consistent and at the same time simple in the interpretation and use of the data, we shall assume that the curvature k is constant throughout the layer which, in some sense, is connected with the asymptotic statement $k\delta \rightarrow 0$. In our case $k\delta = \delta/R \approx 0{\cdot}1$ – not an impressively small number. Nevertheless, we shall assume that our flow field is described by

$$\frac{\partial U}{\partial x}+\frac{\partial V}{\partial y}+kV = 0, \tag{A 1}$$

$$U\frac{\partial U}{\partial x}+V\frac{\partial U}{\partial y}+kUV = -\frac{1}{\rho}\frac{\partial P}{\partial x}+\frac{\partial}{\partial y}\left(\frac{\tau}{\rho}\right)+2k\frac{\tau}{\rho}, \tag{A 2}$$

$$kU_p^2 = \rho^{-1}\frac{\partial P}{\partial y}, \tag{A 3}$$

where $k = k(x)$, P is the mean static pressure and τ is the combined Reynolds shear stress and molecular shear stress. For large y, where $\tau \sim 0$, we have as a solution the irrotational flow field

$$U \sim U_p = U_{pw}(x)\, e^{-k(x)y} \quad \text{as} \quad y \rightarrow \infty, \tag{A 4}$$

or $U_{pw}[(1-ky)+O(yk)^2]$. The full exponential function is, however, operationally convenient.

It will be noted that we are estimating the normal pressure field using $U_p(x,y)$ rather than $U(x,y)$ in (A 3). There are three reasons: first, we believe that the use of (A 3) is a consistent approximation to the boundary-layer equations (where, of course, other terms have been neglected) based on analysis similar to that presented by Yajnik (1970) but more closely related to the analysis of Mellor (1972); second, (A 3) along with (A 1), (A 2) and (A 4) yields a relatively simple momentum integral balance; third, the difference in the calculated profiles is slight. Thus, the relationship between free-stream stagnation pressure and wall static pressure is

$$P_{0\infty}-P(x,0) = \tfrac{1}{2}\rho U_{pw}^2(x). \tag{A 5}†$$

---

† Whereas using $\partial P/\partial y = k\rho U^2$ we would have

$$P_{0\infty}-P(x,0) = \tfrac{1}{2}\rho U_{pw}^2\left[1+2k\int_0^\infty e^{-2ky}\left(\frac{U^2}{U_p^2}-1\right)dy\right].$$

The quantity inside the square brackets is close to unity and varies from 1 to 0·97 for the present data.

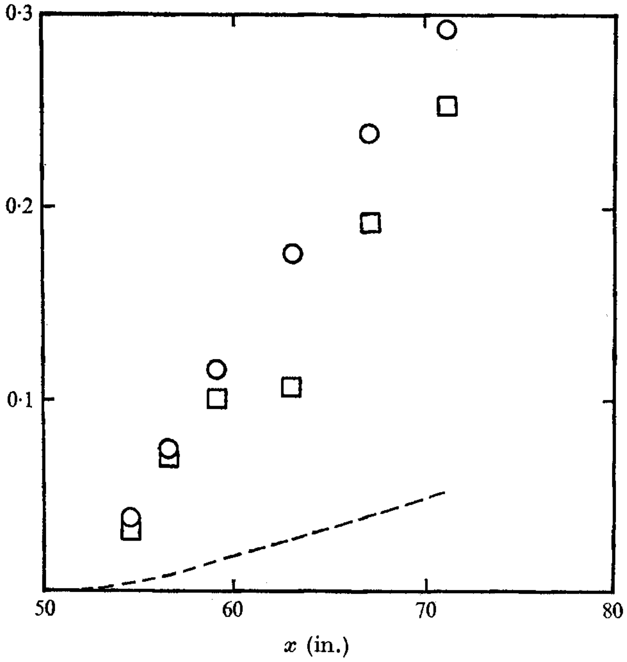

FIGURE 16. Momentum balance. ○, PL, left-hand side of (A 7); □, PR, right-hand side of (A 7); ——, rough estimate of secondary-flow contribution to PR.

From the definition of local stagnation pressure $P_0(x,y) \equiv P(x,y)+\frac{1}{2}\rho U^2(x,y)$, the following equation can be obtained using (A 3) and (A 5):

$$\frac{U^2}{U^2_{pw}} = e^{-2ky} - \frac{P_{0\infty}-P_0(x,y)}{P_{0\infty}-P(x,0)}. \tag{A 6}$$

The first term on the right side of (A 6) is the potential profile and the second the boundary-layer stagnation pressure deficit.

A total head probe shaped like a goose-neck and flattened at the tip to a thickness of 0·008 in. was used to measure $P_{0\infty}-P_0(x,y)$. According to Rogers & Berry (1950) the response of such a flat-nosed probe is quite independent of yaw angles of 15° or less. Therefore, the small yaw angle measured along the tunnel centre-line (figure 3) will not affect the stagnation pressure profile measurements. A pace Model CP 5 ID pressure transducer together with a Disa 55 D 30 digital voltmeter was used to measure the pressure difference. The measured wall static pressure and $P_{0\infty}-P_0(x,y)$ were then substituted into (A 6) to calculate the velocity profiles in figure 8.

Momentum integral balance

The von Kármán momentum integral balance for curved flows can be derived from (A 1)–(A 4) and is

$$\frac{u^2_\tau}{U^2_{pw}} = \frac{d\theta}{dx} + (H+2)\frac{\theta}{U_{pw}}\frac{dU_{pw}}{dx} - q(x)\frac{dk}{dx},$$

where $H \equiv \delta^*/\theta$ and

$$q(x) = \int_0^\infty y\left(1-\frac{U}{U_p}\right)dy + 2\int_0^\infty y\frac{U}{U_p}\left(1-\frac{U}{U_p}\right)dy.$$

Following Coles & Hirst's (1968) procedure, the equation can be written as

$$\int_{x_0}^{x} \frac{u_\tau^2}{(U_{pw}^2)_0} d\left(\frac{x}{\theta_0}\right) = \frac{U_{pw}^2\theta}{(U_{pw}^2\theta)_0} - 1 + \frac{1}{2}\int_{x_0}^{x}\frac{\delta^*}{\theta} d\left(\frac{U_{pw}^2}{(U_{pw}^2)_0}\right) + \frac{1}{(U_{pw}^2\theta)_0}\int_{x_0}^{x}\frac{U_{pw}^2}{R^2}q(x)\,dR(x). \tag{A 7}$$

From the measured values of δ^*, θ and C_f, equation (A 7) is integrated numerically and the result is shown in figure 16. It can be seen that all along the convex test wall PL, denoting the left-hand side of (A 7), is not too much different from PR, denoting the right-hand side of (A 7). Therefore, the two-dimensional momentum integral is satisfied and the flow can be said to be relatively two-dimensional.

The effect of a diverging secondary flow can be included by inserting $\partial W/\partial z$ in (A 1). This adds a term

$$\int_{x_0}^{x}\int_0^\delta \frac{\partial W}{\partial z}\frac{(U_{pw}-U)\,dy\,dx}{(U_{pw}^2\theta)_0}$$

to the right side of (A 7). A rough estimate obtained from the measurements in figure 3 is included in figure 16.

Appendix B. Hot-wire technique

The hot-wire equipment used was one TSI Model 1010 A constant-temperature anemometer; one Disa Model 55 D 10 linearizer; one Disa 55 D 35 true r.m.s. voltmeter; two Disa 55 D 30 digital voltmeters; one Texas Instrument X–Y plotter; one Pace Associates X–Y plotter; and one Techtronic twin-beam oscilloscope. Two hot-wire probes were used: a straight probe, probe A, and a slanted probe, probe B, in which the axis of the stem makes an angle of $\theta = 46°$ with the wall. The characteristic dimensions of the probes are length of stem, 1·5 in.; diameter of stem, 0·059 in.; length of prongs, 0·25 in.; and distance between tips of prongs, 0·06 in. The sensors are tungsten wires mounted with their axes normal to the axis of the stem of the probe. Their characteristic dimensions are diameter 0·00015 in. and sensitive length 0·05 in.

The hot wire was calibrated in a low turbulence calibration tunnel. The maximum turbulence level measured in the tunnel was 0·2 % at a mean flow of 100 ft/s. Calibration of the hot wire was usually made before and after each run, which lasted about 3 h. Practically no change was observed in the calibration curve.

The probes were introduced into the flow through the adjustable wall. Therefore, the stem was positioned normal to the mean flow direction. The disturbances created by the stem and prongs of the probe could influence the measurements. However, Comte-Bellot, Strohl & Alcaraz (1971) found that the net effect caused by positioning the probe in the normal direction was approximately the same as that caused by aligning the probe with the stream direction.

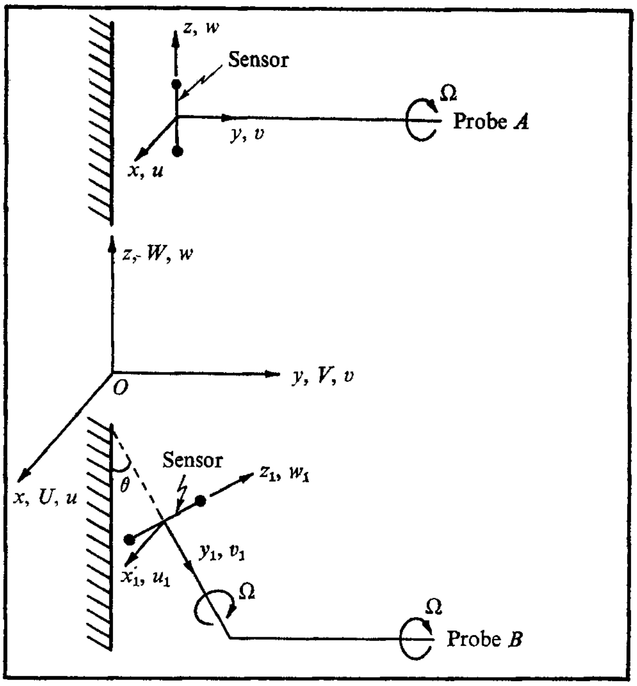

FIGURE 17. Co-ordinate system for probe A and probe B.

In the former case, the net effect was positive, while it was negative in the latter case. The rotation rate was chosen to be $\Omega \sim \frac{1}{12}$ r.p.m. and rotation was taken to span approximately $-\frac{1}{4}\pi < \phi < \frac{1}{4}\pi$. In order to account for the hysteresis due to the different time constants of the low-pass filter and the r.m.s. meter, the recordings were performed in both directions of rotation. The true signal was taken to be the average curve drawn between the two traces.

With probe A, the sensor rotates in a plane that coincides with the x, z plane of a frame of reference attached to the tunnel (figure 17). Therefore the signal gives $\overline{u^2}$, $\overline{uw}$ and $\overline{w^2}$. With probe B, the sensor rotates in a plane that makes an angle of $(\frac{1}{2}\pi - \theta)$ with the x, z plane (figure 17), and the signal gives $\overline{u_1^2}$, $\overline{u_1 w_1}$ and $\overline{w_1^2}$, which resolve to $\overline{u^2}$, $\overline{u(v\cos\theta + w\sin\theta)}$ and $(\overline{v^2}\cos^2\theta + \overline{w^2}\sin^2\theta + 2\overline{vw}\sin\theta\cos\theta)$. With $\overline{u^2}$, $\overline{uw}$ and $\overline{w^2}$ known, $\overline{uv}$ and $\overline{v^2}$ can be calculated from the latter signal provided $\overline{vw}$ is also known.

The general equations derived by Bissonnette & Mellor (1971) were used to analyse the hot-wire signals. Since all measurements were made at the tunnel centre-line, cross flows were very small (figure 3), and for all practical purposes were taken to be zero. Also, in reducing the data for $\overline{uv}$ and $\overline{v^2}$, $\overline{vw}$ was assumed zero. This assumption was justified because of the relative two-dimensionality of the flow. As an independent check, the measured $\overline{uw}$ was found to be quite small (figure 11).

REFERENCES

Bissonnette, L. & Mellor, G. L. 1971 *Princeton University AMS Rep.* no. 1016.

Bradshaw, P. 1969 *J. Fluid Mech.* **36**, 177–191.

Businger, J. A., Wyngaard, J. C., Izumi, Y. & Bradley, E. 1971 *J. Atmos. Sci.* **28**, 181–189.

Clauser, F. 1954 *J. Aero. Sci.* **21**, 91–108.

Clauser, F. H. 1956 *Advances in Applied Mechanics*, vol. 4, pp. 1–51.

Coles, D. C. & Hirst, E. A. 1968 *Computation of Turbulent Boundary Layers. Proc. AFOSR-IFP-Stanford Conference*, vol. 2, pp. 47–54.

Comte-Bellot, G., Strohl. A. & Alcaraz, E. 1971 *J. Appl. Mech.* **38**, 767–774.

Eskinazi, S. & Yeh, H. 1956 *J. Aero. Sci.* **23**, 23–34.

Fujita, H. & Kovasznay, L. S. G. 1968 *Rev. Sci. Inst.* **39**, 1351–1355.

Klebanoff, P. S. 1955 *N.A.C.A. Rep.* no. 1247.

Mellor, G. L. 1967 *A.I.A.A. J.* **5**, 1570–1579.

Mellor, G. L. 1972 *Int. J. Engng Sci.* **10**, 851–873.

Mellor, G. L. & Gibson, D. M. 1966 *J. Fluid Mech.* **24**, 225–253.

Mellor, G. L. & Herring, H. J. 1968 *Computation of Turbulent Boundary Layers. Proc. AFOSR-IFP-Stanford Conference*, vol. 1, pp. 331–345.

Patel, V. C. 1969*a* *Aero. Res. Counc. R. & M.* no. 3599.

Patel, V. C. 1969*b* *Aero. Res. Counc. Current Paper*, no. 1043.

Prandtl, L. 1929 *Sonderdruck aus Vorträge aus dem Gebiete der Aerodynamik und verwandter Gebiete.* Aachen. (See also 1931 *N.A.C.A. Tech. Memo.* no. 625.)

Reynolds, O. 1884 *Scientific Papers*, vol. 2, p. 157. Cambridge University Press.

Rogers, E. W. E. & Berry, C. J. 1950 *Aero. Res. Counc. Rep. Current Paper*, no. 41.

Schmidbauer, H. 1936 *N.A.C.A. Tech. Memo.* no. 791.

Schneider, W. G. & Wade, J. H. T. 1967 *Can. Aero. & Space J.* **13**, 73–89.

So, R. M. C. & Mellor, G. L. 1972 *N.A.S.A. Contractor Rep.* no. 1940.

Wattendorf, F. L. 1935 *Proc. Roy. Soc.* A **148**, 565–598.

Wilcken, H. 1930 *Ing. Arch.* **1**, 358–376.

Yajnik, K. S. 1970 *J. Fluid Mech.* **42**, 411–427.